Chapter-3 Thermal Conductivity of MoS_2 Nanostructures using Optothermal Raman Spectroscopy Technique

3.1 Introduction

As a basic physical property, thermal behaviour of any 2D material has been vital in its application and energy conversion in thermoelectric [146]. Hence, there have been multiple efforts to investigate and examine the thermal transport in 2D materials for the purpose of fundamental research and applications. The 2D materials display distinctive thermal behaviour from their bulk counterparts, such as ballistic and hydrodynamic transport of phonons at low temperatures [68, 147, 148]. The 2D materials having novel phonon properties, high thermal conductivity, and good mechanical flexibility can be useful for both fundamental studies of heat transfer and thermal management in next-generation device applications. In electronic and optoelectronic devices, generated heat increases their operating temperature and effect the performance of electronic device. The heat conduction study in 2D systems is at early stage due to the technical challenges in preparing 2D materials suitable for thermal measurements. The 2D materials such as MoS_2 nanostructures are used on certain substrates like SiO_2/Si or Si substrates and hence understanding of thermal transport properties of substrate supported MoS_2 nanostructures is essential for thermal management in those devices along with their electronic properties. Different techniques have been used for identifying the thermal conductivity of materials such as Optothermal Raman technique (OTR) [51], Thermal bridge method with prepatterned built-in microstructures [73], 3ω method [74], Time-domain thermo reflectance (TDTR) method [75], Scanning thermal microscope (SThM) [76] and Thermal flash method [77]. Among these methods, optothermal Raman (OTR) technique

is mostly used to determine the thermal conductivity of low dimensional materials (1D and 2D). In this technique, excitation laser source acts as a heat source to produce a local temperature rise in the film, kept in ambient conditions (room temperature and atmospheric pressure). As the laser power increases, the Raman active modes show red shifting due to the thermal softening effect. Further, shift in Raman modes is also observed at fixed laser power and at different sample temperature using thermal stage. Thermal modelling can then be used to determine the thermal conductivity from the measured shift rate [149, 150]. The combination of temperature and power dependence of optical phonon frequencies allows estimation of thermal conductivity. The schematic diagram of OTR technique is shown in **Figure 3.1**.

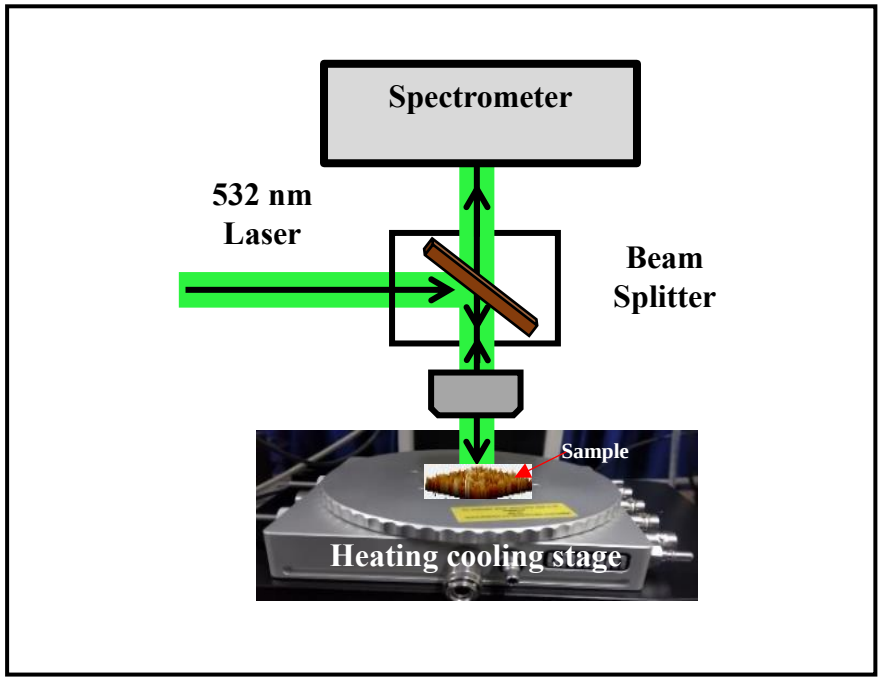

Figure 3.1. *Schematic representation of optothermal Raman technique.*

There have been few studies on understanding thermal transport in monolayer and few-layers MoS_2 nanostructures using OTR study [51, 151, 152]. Yuan *et al.* prepared eight different thickness 2.4, 3.6, 5.0, 9.2, 15.0, 24.6, 30.6 and 37.8 nm of MoS_2 over glass substrate and found the corresponding thermal conductivities to be 60.3, 46.0, 35.1,

31.0, 51.0, 52.4, 62.9 and 76.2 W m^{-1} K^{-1}, respectively [151]. They showed that thermal conductivity decreases with increasing thickness up to a certain thickness (9.2 nm) and beyond that increases with increasing thickness. Taube *et al.* calculated the thermal conductivity of monolayer MoS_2 supported over SiO_2/Si substrate and found thermal conductivity of 62.2 W m^{-1} K^{-1} at room temperature (300 K). They also observed the decrease in thermal conductivity with temperature having thermal conductivity of 7.45 W m^{-1} K^{-1} at 450 K [152]. Zhang *et al.* studied thermal conductivity of monolayer and bi-layer MoS_2 by refine optothermal method. They found thermal conductivity values to be ~ 84±17 and ~77±25 W m^{-1} K^{-1} for suspended monolayer and bi-layer MoS_2, respectively. They also calculated thermal conductivity of supported MoS_2 over gold coated SiO_2/Si substrate, and found thermal conductivities of 55±20 and 35±7 W m^{-1} K^{-1} for monolayer and bi-layer case, respectively [51]. These studies clearly show that supported MoS_2 structure exhibits lower thermal conductivity compared to the suspended one due to the strain effect of substrate. In the present work, we have calculated thermal conductivities of triangular bi-layer MoS_2 over SiO_2/Si substrate and vertically oriented few-layer (VFL) MoS_2 film over Si substrate using OTR technique. We have discussed the strain effect due to the substrate in MoS_2 nanostructure and its effect on thermal conductivity. In the past, mostly thermal conductivity of suspended and supported monolayer and few-layer mechanically exfoliated horizontal MoS_2 nanostructures have been studied. In the present work, we demonstrate the thermal conductivity measurement of CVD grown horizontal bi-layer MoS_2 and vertically grown few-layer MoS_2.

3.2 Results and Discussion

3.2.1 Thermal Conductivity of Triangular Supported Bi-Layer MoS_2

This section deals with the characterization and investigation of thermal properties of horizontally grown triangular bi-layer MoS_2 over SiO_2/Si substrate. Temperature and power dependent Raman studies have been performed to determine the thermal conductivity of SiO_2/Si supported triangular bilayer MoS_2 film.

3.2.1.1 Characterization of Triangular Bi-Layer MoS_2

The large area optical image of growth region of bi-layer MoS_2 over SiO_2/Si is shown in **Figure 3.2 (a)**, which indicates the dimension of each triangular MoS_2 in the range 10-20 µm. The Raman spectrum of triangular bi-layer MoS_2 film over SiO_2/Si substrate is shown in **Figure 3.2 (b)**, indicating two peaks at ~383.7 and ~404.2 cm^{-1} corresponding to the E^1_{2g} and A_{1g} modes, respectively. The E^1_{2g} mode represents the in-plane vibration of Mo and S atoms in opposite direction and A_{1g} mode represents the out of plane vibration of S atoms only. A sharp intense peak around 520.5 cm^{-1} corresponds to silicon, originating from the substrate. The inset image of **Figure 3.2 (b),** shows the fitting of both the Raman peaks and separation between these two Raman modes (E^1_{2g} and A_{1g}) is observed around 20±0.5 cm^{-1}, suggesting the presence of two layers in prepared triangular MoS_2 [14, 153]. We observe the morphology and height profile of the prepared triangular MoS_2 on SiO_2/Si substrate using atomic force microscopy (AFM). The AFM image of (**Figure 3.2 c**), shows the growth of triangular MoS_2 with thickness around 1.6 nm in (**Figure 3.2 d**) confirming the presence of two layers in MoS_2 [37].

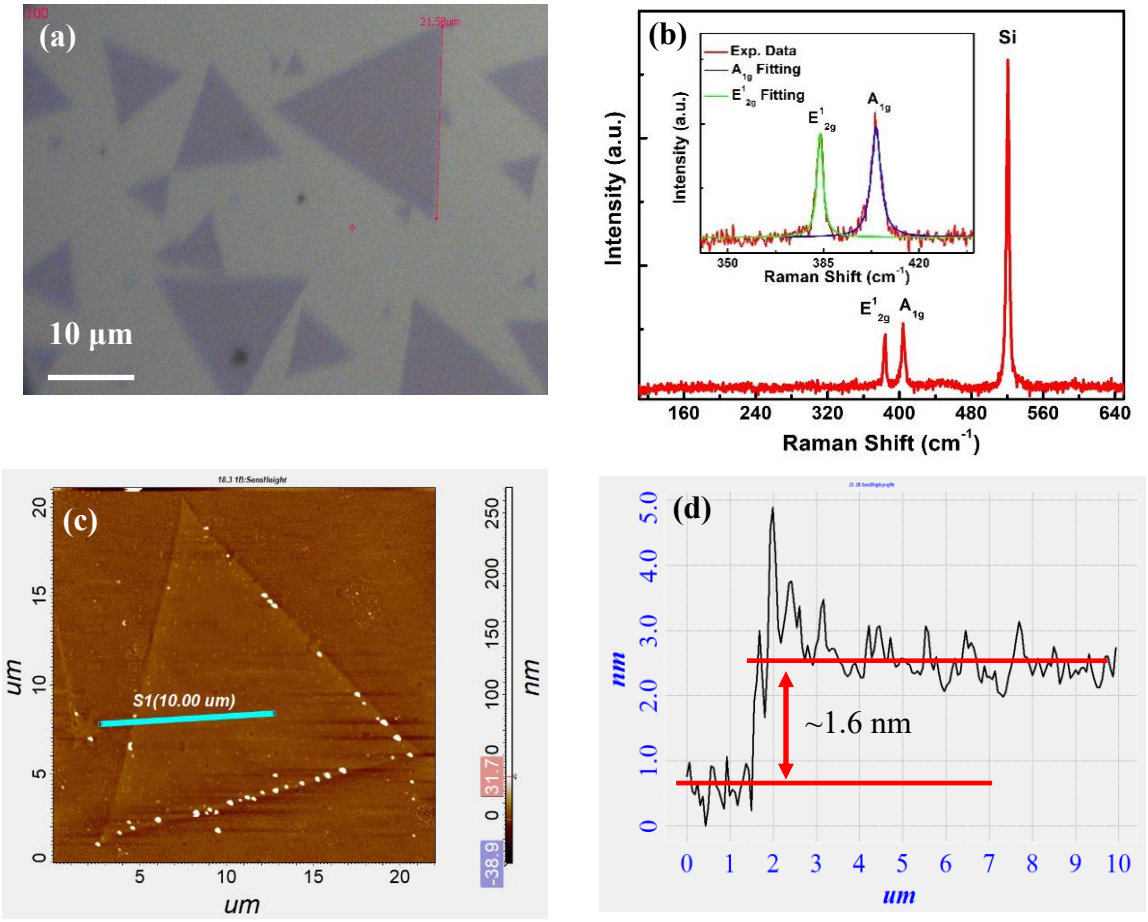

Figure 3.2 *(a) Optical image, (b) Raman spectrum (Lorentzian fitting of A_{1g} and E^1_{2g} as inset, (c) AFM image and (d) Corresponding height profile of triangular bi-layer MoS_2 over SiO_2/Si substrate.*

3.2.1.2 Calculation of Thermal Conductivity of Supported Bi-Layer MoS_2 Film

In order to determine the thermal conductivity (k_s) of SiO_2/Si supported bi-layer MoS_2, OTR technique has been applied, which comprises of temperature and power dependent Raman studies. The temperature distribution in MoS_2 can be obtained from the heat diffusion equation in cylindrical coordinates as per following form [78, 149] -

$$\frac{1}{r}\frac{d}{dr}\left(r\frac{dT(r)}{dr}\right) - \frac{g}{k_s t}(T(r)-T_{amb}) = -\frac{Q}{k_s} \qquad (3.1)$$

where T(r) and r are the temperature distribution and radial position measured from the centre of the laser beam, respectively. Here, T_{amb} is the ambient temperature, t is the

thickness of the film, k_s is the thermal conductivity of supported film and g is the total interfacial thermal conductance per unit area. Q is the volumetric optical heating, which is given by

$$Q = \frac{q_0 \alpha}{t} \exp\left(-\frac{r^2}{r_0^2}\right) \quad (3.2)$$

where q_0, α and r_0 are the maximum absorbed laser power per unit area, absorption coefficient of the material and the radius of the laser beam spot, respectively. The total absorbed laser power P_{abs} is given by-

$$P_{abs} = \int_0^{\infty} q_0 \exp\left(-\frac{r^2}{r_0^2}\right) 2\pi r \, dr = q_0 \pi r_0^2$$

By considering $\theta(r) = T(r) - T_{amb}$ and $z = \left(\frac{g}{k_s t}\right)^{1/2} r$, **equation 3.1** becomes-

$$\frac{d^2\theta}{dz^2} + \frac{1}{z}\frac{d\theta}{dz} - \theta = -\frac{q_0}{g} \exp\left(-\frac{z^2}{z_0^2}\right) \quad (3.3)$$

The analytical solution for the supported film can be written as-

$$\theta(z) = C_1 I_0(z) + C_2 K_0(z) + \theta_P(z) \quad (3.4)$$

where I_0 and K_0 are zero-order modified Bessel functions of the first and second kind, respectively. In the **equation 3.4**, $\theta_P(z)$ is denoted as the particular solution of nonhomogeneous differential equation and can be written as follows-

$$\theta_P(z) = I_0(z) \int K_0(z) \frac{\frac{q_0}{g}\exp\left(-\frac{z^2}{z_0^2}\right)}{-I_0(z)K_1(z) - K_0(z)I_1(z)} dz - K_0(z) \int I_0(z) \frac{\frac{q_0}{g}\exp\left(-\frac{z^2}{z_0^2}\right)}{-I_0(z)K_1(z) - K_0(z)I_1(z)} dz \quad (3.5)$$

where $I_1(z)$ and $K_1(z)$ are the first-order modified Bessel functions of the first and second kind, respectively. To obtained the value of C_1 and C_2 in **equation 3.4**, we have incorporated the following boundary conditions-

$$\frac{d\theta}{dz} = 0 \; at \; z = 0,$$

$$\theta(z) = 0 \; at \;\; z \rightarrow \infty$$

After using these boundary conditions, we get $C_2 = 0$ and $C_1 = -\lim_{z\to\infty} \frac{\theta_P(z)}{I_0(z)}$, which approaches a constant value for large z.

Now, $\theta(z) = -I_0(z) \lim_{z\to\infty} \frac{\theta_P(z)}{I_0(z)} + \theta_P(z)$

The temperature rise in 2D film, measured by the Raman laser beam can be given by-

$$\theta_m = \frac{\int_0^\infty \theta(r) \exp\left(-\frac{r^2}{r_0^2}\right) r \, dr}{\int_0^\infty \exp\left(-\frac{r^2}{r_0^2}\right) r \, dr} \tag{3.6}$$

Then, the thermal resistance of the supported film is defined as R_m and it is the ratio of θ_m and P_{abs}. It can be expressed as follows-

$$R_m = \frac{\theta_m}{P_{abs}} = \frac{\int_0^\infty \left[-I_0(z) \lim_{z\to\infty} \frac{\theta_P(z)}{I_0(z)} + \theta_P(z)\right] \exp\left(-\frac{r^2}{r_0^2}\right) r \, dr}{\int_0^\infty \exp\left(-\frac{r^2}{r_0^2}\right) r \, dr \int_0^\infty q_0 \exp\left(-\frac{r^2}{r_0^2}\right) 2\pi r \, dr} \tag{3.7}$$

where, R_m is the function of r_0, k_s and g. To avoid the artificial shift in mode frequency we have used $R_m = \frac{\partial \theta_m}{\partial P_{abs}}$

At the same time, R_m can be experimentally obtained using the following relation [59]

$$R_m = \chi_P / \alpha \chi_T \tag{3.8}$$

where χ_P and χ_T are first order power and temperature coefficients of the material. Where α is the absorption coefficient and is assumed to be around 0.115 for bi-layer MoS_2 as per literature reports [51]. In order to get the value of R_m we need the value of χ_T and χ_P, which can be determine by temperature and power dependent Raman studies, respectively. The temperature and power dependent Raman studies of bi-layer MoS_2 have been discussed below.

Temperature Dependent Raman Study

We have examined the thermal response to phonon confinement in MoS_2 for analyzing its thermal transport properties. Such studies are of fundamental importance for the effect of an in-depth understanding of the lattice potential energy, vibrations, thermal expansion, and thermal conductivity of MoS_2. These thermal properties of material play a vital role in determining the efficiency of their electronic and optoelectronic devices [47, 154]. Schematic diagram of temperature dependent Raman study of bi-layer MoS_2 is shown in **Figure 3.3 (a)**. The temperature-dependent Raman shift is used to investigate different properties such as phonon-phonon and electron-phonon interactions [78]. The temperature-dependent Raman spectra of triangular bi-layer MoS_2 film over SiO_2/Si substrate using LWD 50x objective lens are taken from near liquid-nitrogen temperature (~83 K) to room temperature (300 K), as shown in **Figure 3.3 (b)**. We observe strong scattering intensity of both the Raman modes E^1_{2g} and A_{1g} throughout the temperature range and both the Raman modes soften linearly with the temperature. This softening interprets the electron-phonon interaction and the anharmonicity among phonons [71]. **Figure 3.3 (c)** shows the temperature dependence of the Lorentzian-fit peak frequencies of supported bi-layer MoS_2 in temperature range 83 K to 300 K for the A_{1g} (black squares) and E^1_{2g} (red circles) phonons. The peak position ω (in cm^{-1}) follows linear dependence and can be expressed as follows [78] -

$$\omega(T_2) - \omega(T_1) = \chi_T(T_2 - T_1) \tag{3.9}$$

where χ_T and T represents the first-order temperature coefficient and absolute temperature, respectively. We find χ_T to be -0.011 ± 0.0005 and -0.009 ± 0.0003 cm^{-1} K^{-1} for A_{1g} and E^1_{2g} modes, respectively, using LWD 50x objective lens. The linear variation of phonon frequency in bi-layer MoS_2 on SiO_2/Si substrate is due to the anharmonic vibrations of lattice [152]. The lattice expands or contracts due to temperature variation,

the equilibrium positions of atoms and consequently the interatomic forces change, which create shifts in phonon energies [80]. **Figure 3.3 (d)** shows the variation of FWHM for both the Raman modes and as expected FWHM increases with temperature. Hence, we observe that phonon confinement in bi-layer MoS_2 is highly sensitive to thermal energy, suggesting good thermal transport behaviour of prepared bi-layer MoS_2. Larger values of χ_T and the slope of FWHM versus temperature for A_{1g} mode suggests that interlayer coupling is more sensitive and responsible for thermal transport in prepared bi-layer MoS_2 over SiO_2/Si substrate as E^1_{2g} mode is affected by substrate's strain.

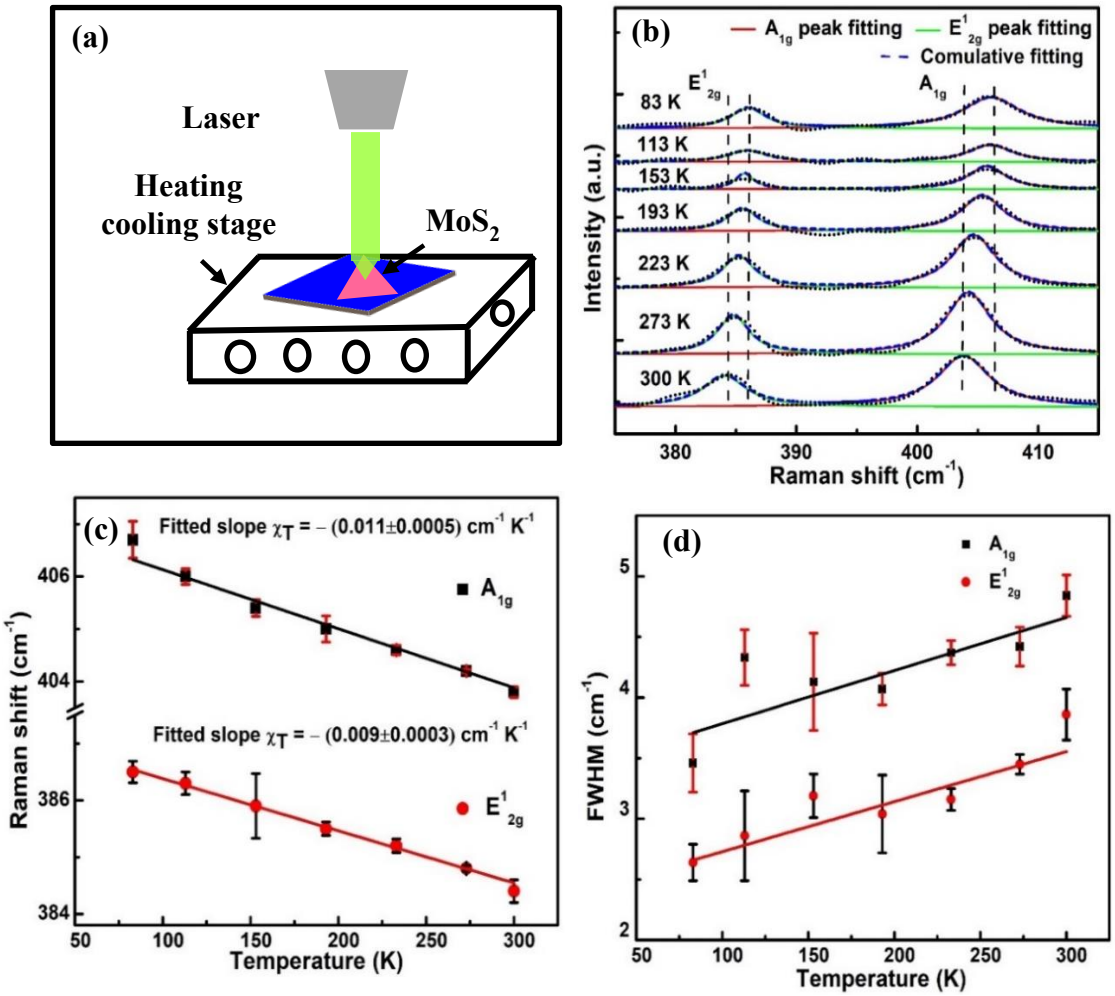

Figure 3.3 *(a) Schematic diagram of temperature dependent Raman study. (b) Temperature dependent Raman spectra of triangular bi-layer MoS_2 on SiO_2/Si substrate using LWD 50x. Variations of (c) Peak position and (d) FWHM with respect to temperature of triangular bi-layer MoS_2 on SiO_2/Si substrate.*

Power Dependent Raman Study

In order to calculate thermal conductivity of supported bi-layer MoS_2, we have further examined the local temperature rise in terms of phonon confinement by heating with different laser power. The schematic diagram for power dependent Raman study is shown in **Figure 3.4 (a)**. The laser light falls on the top of MoS_2 sample and produces the shifting in the Raman modes due to the local heating. The power dependent Raman spectra using LWD 50x objective lens are shown in **Figure 3.4 (b)**. We observe that the intensity increases for both the Raman peak and red shifting is observed with increasing laser power due to the softening of bonds via local temperature rise in MoS_2 [79]. The Lorentzian peak fitting provides the Raman peak positions for both modes as a function of incident laser power, as shown in **Figure 3.4 (c)**. The linear change in peak position with the laser power can be expressed as follows [78]

$$\omega(P_2) - \omega(P_1) = \chi_P(P_2 - P_1) \tag{3.10}$$

where χ_P and P indicate first-order power-dependent coefficient and incident laser power on the top of the sample, respectively. The χ_P values are found to be -0.963±0.18 and -0.635±0.11 cm^{-1} mW^{-1} for A_{1g} and E^1_{2g} modes, respectively, using LWD 50x objective lens. Experimentally it is observed that the A_{1g} mode is less effected by the substrate as compared to the in-plane mode E^1_{2g} mode as suggested by lower value of power coefficient (χ_P) for E^1_{2g} mode as compared to that for A_{1g} mode. Hence, thermal transport behaviour of supported film is usually examined by A_{1g} mode [51]. We also find that the FWHM of both the Raman peaks increases with the incident laser power as shown in **Figure 3.4 (d)**. The observed red shift in Raman modes and increase in FWHM with laser power can be directly attributed to the lattice expansion and softening of bonds [79].

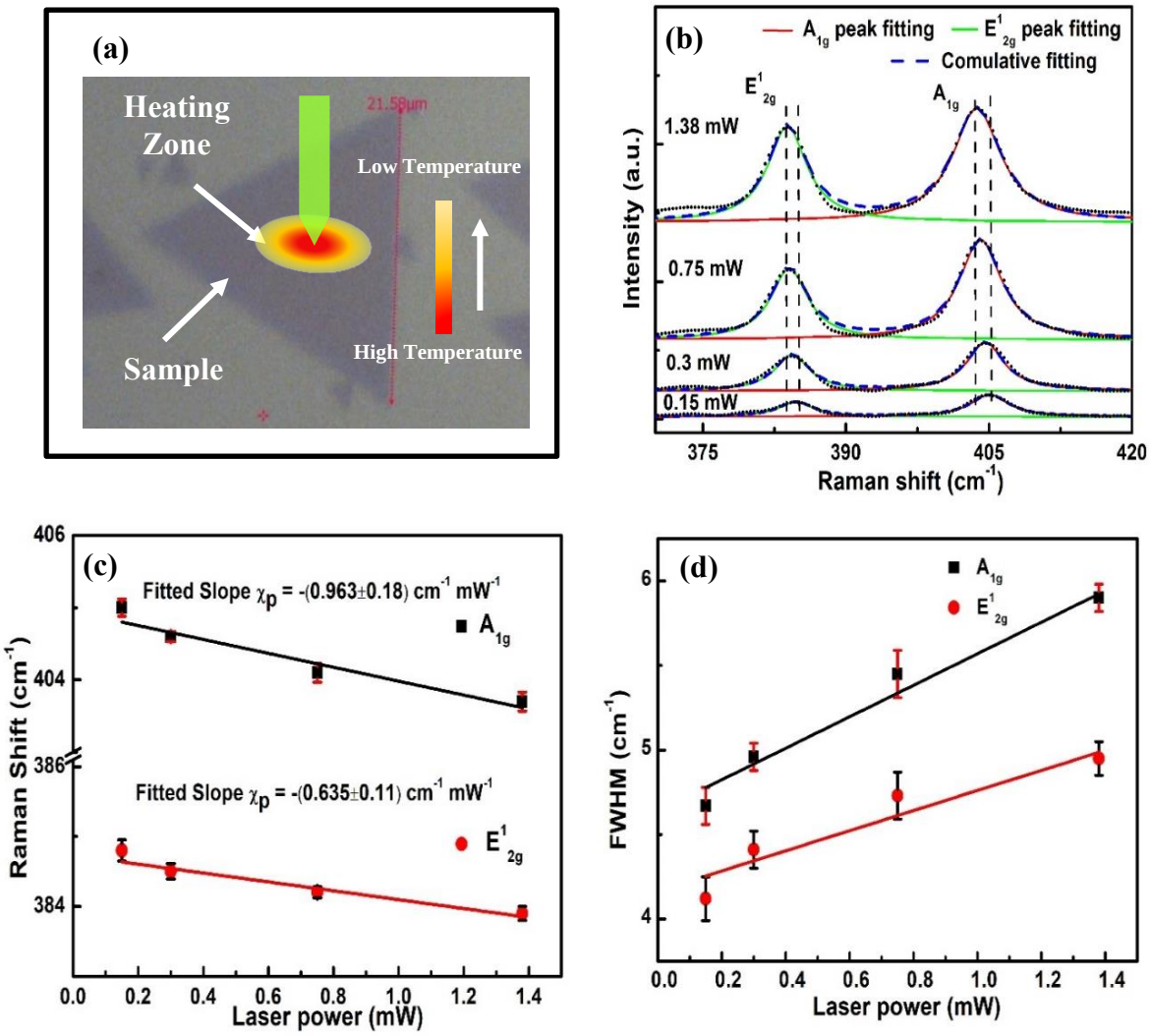

Figure 3.4 *(a) Schematic diagram of power dependent Raman study. (b) Power dependent Raman spectra of triangular bi-layer MoS_2 on SiO_2/Si substrate using LWD 50x lens. Variations of (c) Peak position and (d) FWHM with incident laser power for triangular bi-layer MoS_2.*

In case of LWD 50x objective lens, the values of χ_P and χ_T for the A_{1g} mode are 0.963 cm^{-1} mW^{-1} and 0.011 cm^{-1} K^{-1}, respectively. The corresponding R_m value is calculated ~ 7.6126×10^5 K W^{-1} using **equation 3.8**. The absorption coefficient (α) is assumed to be around 0.115 for bi-layer MoS_2 as per literature reports [51]. In order to solve the **equation 3.1** to **equation 3.7**, we have used the method described by Cai *et al.* which yields a value of R_m that is a function of k_s and g [149]. Moreover, the ratio of R_m for the two different spot sizes is a function of the ratio g/k_s. In order to get the unique value of k_s and g, we need to have at least two different values of R_m in different

experimental condition. We have performed the temperature and power dependent Raman studies of bi-layer MoS_2 with another objective lens of 100x to calculate different value of R_m. The temperature dependent Raman spectra of supported bi-layer MoS_2 taken under 100x objective lens in temperature range 153-303 K are shown in **Figure 3.5 (a)**. The corresponding peak positions for the A_{1g} (black squares) and E^1_{2g} (red circles) phonons modes at different temperatures are found varying linearly as shown in **Figure 3.5 (b)**. We find first-order temperature coefficient (χ_T) to be −0.014±0.0008 and −0.011±0.0003 cm^{-1} K^{-1} for A_{1g} and E^1_{2g} modes, respectively, using **equation 3.9**.

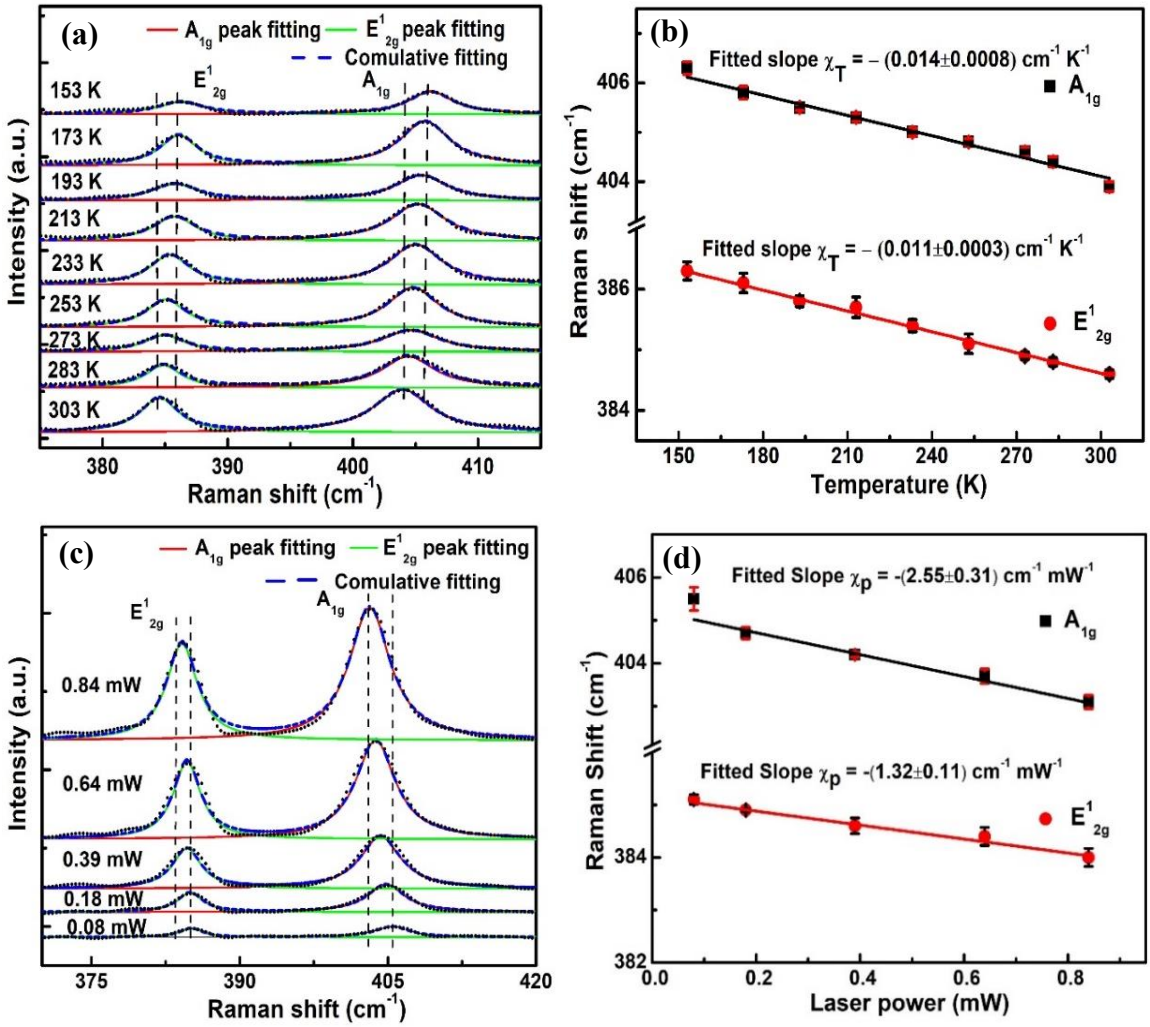

Figure 3.5 *(a) Temperature dependent Raman spectra of triangular bi-layer MoS_2 on SiO_2/Si substrate using 100x objective lens. (b) Variation of peak position with respect to temperature. (c) Power dependent Raman spectra of triangular bi-layer MoS_2 on SiO_2/Si substrate using 100x objective lens. (d) Variation of peak position with respect to laser power.*

The power dependent Raman spectra using 100x objective lens are shown in **Figure 3.5 (c)** and the corresponding linear shift in Raman peak positions is shown in **Figure 3.5 (d)**. The first-order power-dependent coefficient (χ_P) values are found to be -2.55±0.31 and -1.32±0.11 cm^{-1} mW^{-1} for A_{1g} and E^1_{2g} modes, respectively, using **equation 3.10**. In 100x objective lens the values of χ_P and χ_T for A_{1g} mode are 2.55 cm^{-1} mW^{-1} and 0.014 cm^{-1} K^{-1} respectively, and the corresponding R_m is found to be 15.8385×10^5 K W^{-1} using **equation 3.8**. The radius of laser spot size for each objective lens is calculated using following equation [78, 155, 156] -

$$r_0 = \frac{\lambda}{\pi \times NA}\, nm \tag{3.11}$$

where λ and NA represents the wavelength of the laser light and numerical aperture of the objective lens, respectively. The parameter r_0, is the Gaussian beam radius or minimum laser spot size. We have calculated the radius of the laser spot size using above **equation 3.11** for 100x (NA=0.9) and LWD 50x (NA=0.6) objective lenses around 0.19×10^{-6} m and 0.28×10^{-6} m, respectively, with 532 nm laser. For the supported bi-layer MoS_2, we have found the experimental value of R_m~ 15.8385×10^5 K W^{-1} and 7.6126×10^5 K W^{-1} for spot size 0.19×10^{-6} m (100x objective lens) and 0.28×10^{-6} m (LWD 50x objective lens), respectively. By solving **equation 3.1** to **equation 3.7** using MATLAB program, we find unique values of g~ 1.264 ± 0.128 MW m^{-2} K^{-1} and k_s~ 42 ± 8 W m^{-1} K^{-1} for SiO_2/Si supported triangular bi-layer MoS_2 film. The low value of interfacial thermal conductance can be attributed to the lattice mismatch between MoS_2 and substrate [157]. The value of 'g' also decreases with increasing thickness of SiO_2 in the substrate [84]. Since the interfacial thermal conductance has been calculated using thermal model in which, the absorbed heat mostly transfers radially through in-plane direction and less in the cross-plane direction, it may also lead to low value of 'g' [51,

152, 157]. In summary, the low value of 'g' can be attributed to the possible lattice mismatch between substrate and MoS_2, large thickness of SiO_2 (~285 nm) in SiO_2/Si substrate and the used heat diffusion model for calculating thermal conductivity of the film [84, 157]. The high value of k_s can be associated with better in-plane thermal transport due to high quality of prepared bi-layer MoS_2, which reduces the phonon-defect scattering [158].

3.2.2 Thermal Conductivity of Vertically Oriented Few-Layer MoS_2 Film

We have also studied the thermal conducting behaviour of CVD grown vertically oriented few-layer (VFL) MoS_2 film over Si substrate using OTR technique. In the previous section, we have discussed about the thermal conductivity of horizontally grown bi-layer MoS_2 film over SiO_2/Si substrate. In that case, horizontally grown bi-layer MoS_2 and substrate are in contact throughout the region and hence their thermal transport behaviour is under maximal strain resulting in its lower thermal conductivity [51, 83]. However, this strain is minimal for vertically oriented MoS_2 due to much smaller contact area between MoS_2 and Si substrate and hence, this VFL-MoS_2 can be treated as a free-standing film or suspended film. In the following section, we have investigated the thermal transport behaviour of VFL-MoS_2 by treating it as a suspended film.

3.2.2.1 Characterization of VFL-MoS_2 Film

Surface morphology of the VFL-MoS_2 film was characterized by High resolution scanning electron microscopy (HRSEM) and Atomic force microscopy (AFM) studies. **Figure 3.6 (a)** shows the SEM image of VFL-MoS_2, indicating the presence of interconnected vertically oriented MoS_2 nanosheets over Si substrate. It indicates the lateral dimension around 400 nm with ultrathin layers having significant transparency.

Figure 3.6 (b) shows the AFM image of VFL-MoS_2 indicating the growth of MoS_2 in the vertical direction with average height around 500 nm, as shown in **Figure 3.6 (c)**.

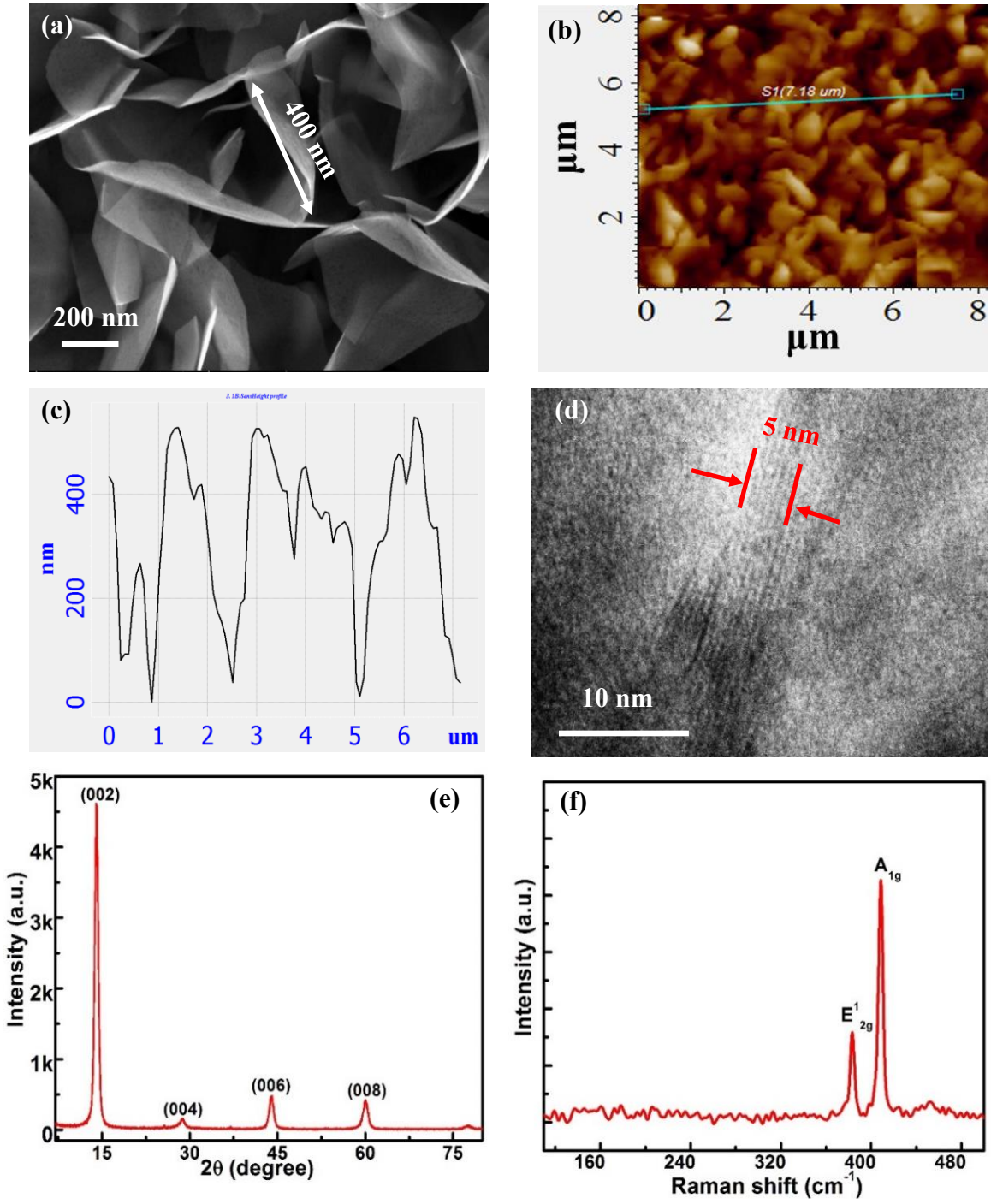

Figure 3.6 *(a) HRSEM (b) AFM (2D view) and (c) Height profile of VFL-MoS_2 over Si-substrate. (d) HRTEM image of edge cross sectional view of VFL-MoS_2 (e) XRD pattern and (f) Raman spectrum of VFL-MoS_2.*

Figure 3.6 (d) shows the high-resolution TEM (HRTEM) image of VFL-MoS_2, depicting the presence of 5 nm thick (containing 6-7 layers) vertical MoS_2 nanostructures and suggesting interlayer spacing ~ 0.67 nm. The crystalline nature of VFL-MoS_2 has been further confirmed by X-ray diffraction (XRD) study. **Figure 3.6 (e)** shows the XRD diffraction peaks of VFL-MoS_2 at different angle, 2θ = 14.06°, 28.75°, 43.97°, and 60.02°, corresponding to (002), (004), (006) and (008) for VFL-MoS_2 (JCPDS card No. 37-1492), respectively. The XRD pattern suggests the orientation of individual MoS_2 nanosheets in [001] direction, as reported in literature for 2D materials with a vertical orientation [96, 159]. The first-order Raman spectrum of VFL-MoS_2 (**Figure 3.6 f**) shows in-plane E^1_{2g} (~ 383 cm^{-1}) and out-of-plane A_{1g} (~ 408 cm^{-1}) optical phonon modes at the Brillouin zone centre. The separation of 25 cm^{-1} is observed in Raman modes and thickness of the MoS_2 flake is found around 5 nm by HRTEM study, indicating the possibility of six to seven layers as suggested in literature [96].

3.2.2.2 Calculation of Thermal Conductivity of VFL-MoS_2 Film

The thermal conductivity (k) of VFL-MoS_2 film was extracted from OTR technique. Since there is minimum contact area between VFL-MoS_2 and the Si substrate, hence it can be treated as free standing or suspended film and the interfacial thermal conductance would be zero [79]. Therefore, in this case we consider different model to calculated the thermal conductivity. The strain is minimal for VFL-MoS_2 and hence it may provide better thermal transport. The conduction of heat (Q) through a plane laminar surface having cross sectional area A over the time (t) can be expressed through the following equation [79]-

$$\frac{\partial Q}{\partial t} = -k \oint \nabla T \cdot dA \tag{3.12}$$

where k is the thermal conductivity of the film and T is the absolute temperature. A plane

wave heat flow can be considered for thermal conductivity of suspended film using following equation [72, 160] -

$$k = \chi_T\left(\frac{L}{2hW}\right)\left(\frac{\delta\omega}{\delta P}\right)^{-1} \quad (3.13)$$

where 2L is the lateral dimension of suspended flake, χ_T is the first order temperature coefficient, δω is the Raman peak shift due to the variation δP in the incident laser power which causes heating on the sample surface. This δω/δP is equivalent to χ_P, the first order power coefficient. For a suspended 2D film cross trench having width greater than the laser spot size, it is assumed that heat spreads from the centre in two opposite directions. Hence, thermal conductivity can be evaluated using following expression [72, 160] -

$$k = \left(\frac{L}{2hW}\right)\left(\frac{\chi_T}{\chi_P}\right) \quad (3.14)$$

where h is the thickness and W is the width of each flake.

Temperature Dependent Raman Study of VFL-MoS_2

Thermal response of vibrational modes can help to interpret anharmonicity among phonons and electron-phonon interactions of VFL-MoS_2 and its thermal properties [78, 79]. **Figure 3.7 (a)** shows the schematic representation of temperature dependent Raman study of VFL-MoS_2. The temperature-dependent Raman study was performed from ~83 K to ~453 K using LWD 50x objective lens. We observe strong scattering intensity of E^1_{2g} and A_{1g} Raman mode throughout the temperature range and these two Raman modes soften linearly with the temperature. Raman spectra of VFL-MoS_2 at different temperatures indicates the peaks shift (by Lorentzian peak-fitting) with temperature as shown in **Figure 3.7 (b)**. The linear shifts in the Raman peaks positions ω (in cm^{-1} units) as a function of temperature are shown in **Figure 3.7 (c)**. The lattice expands with temperature due to the anharmonicity of the interatomic potential, which induces a shift

in the phonon energies, observed as linear red shift for A_{1g} and E^1_{2g} mode [79]. The linear temperature coefficients (χ_T) for the A_{1g} and E^1_{2g} modes using **equation 3.9** are found to be -0.011±0.001 and -0.012±0.001 cm^{-1} K^{-1}, respectively. The basal plane of VFL-MoS_2 is in the perpendicular direction to the substrate and hence substrate will have minimal influence (strain) on both (E^1_{2g} and A_{1g}) modes suggesting suspended like behaviour of VFL-MoS_2. **Figure 3.7 (d)** shows the variation of FWHM for both the Raman modes indicating the increase of FWHM with temperature, which can be attributed to the softening of the bonds and the lattice dilation [79].

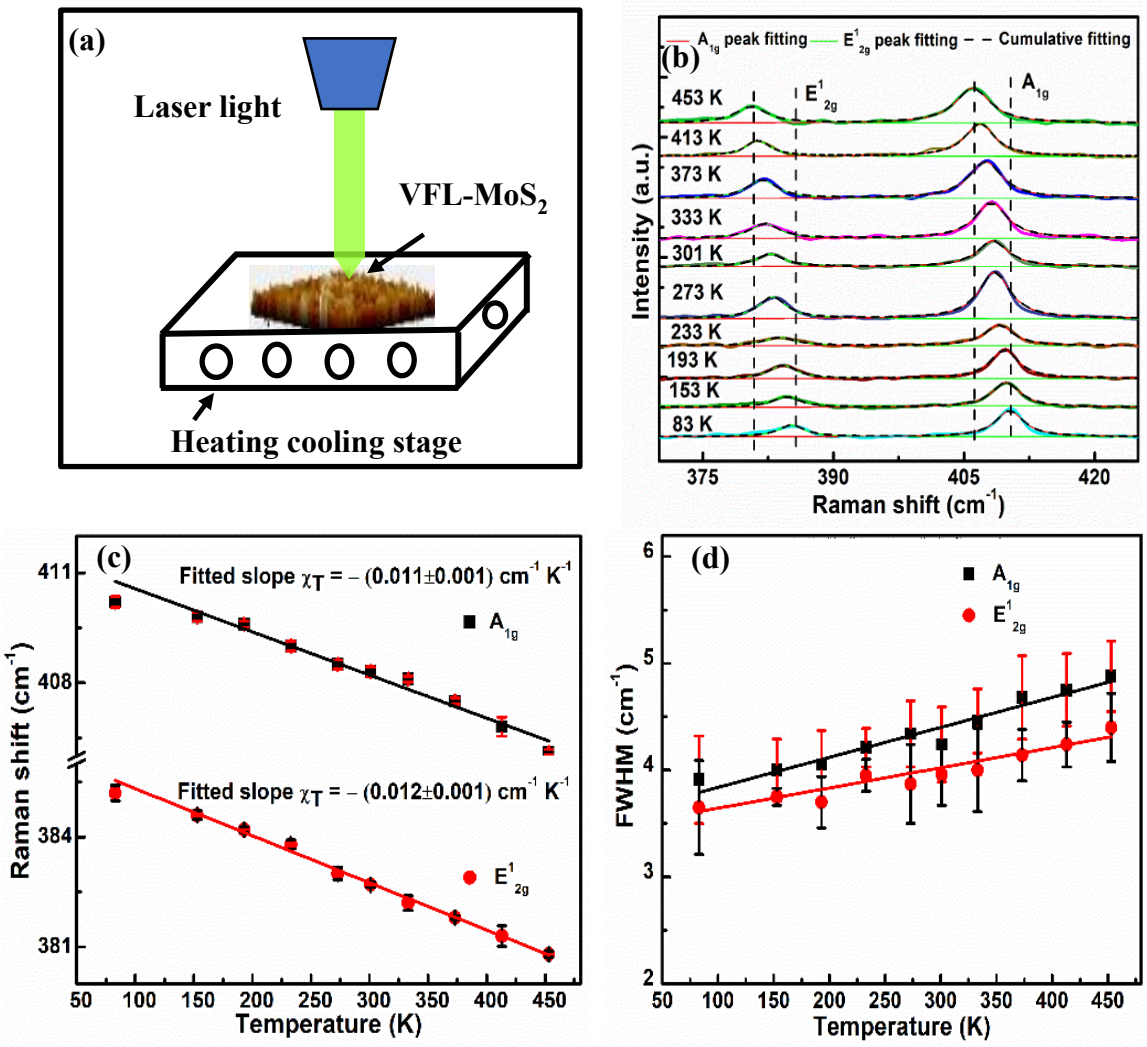

Figure 3.7 *(a) Schematic of temperature dependent Raman study of VFL-MoS_2 (b) Raman spectra of VFL-MoS_2 at different temperatures (c) Raman shifts and (d) FWHM of E^1_{2g} and A_{1g} modes as a function of temperature.*

Power Dependent Raman Study of VFL-MoS_2

In order to calculate the thermal conductivity of VFL-MoS_2, we have further performed power dependent Raman study to observe phonon confinement by local heating with different laser power, as shown schematically in **Figure 3.8 (a)**. Our grown VFL-MoS_2 film is an interconnected network of few-layer MoS_2 nanosheets and this structure indicates the possibility of multiple reflection of laser light resulting in nearly full absorption of the incident light. Hence, incident power can be treated as an absorbed power in this case, where the incident laser light produces maximum heating at the centre. We have performed the Raman spectra of VFL-MoS_2 at different incident laser powers.

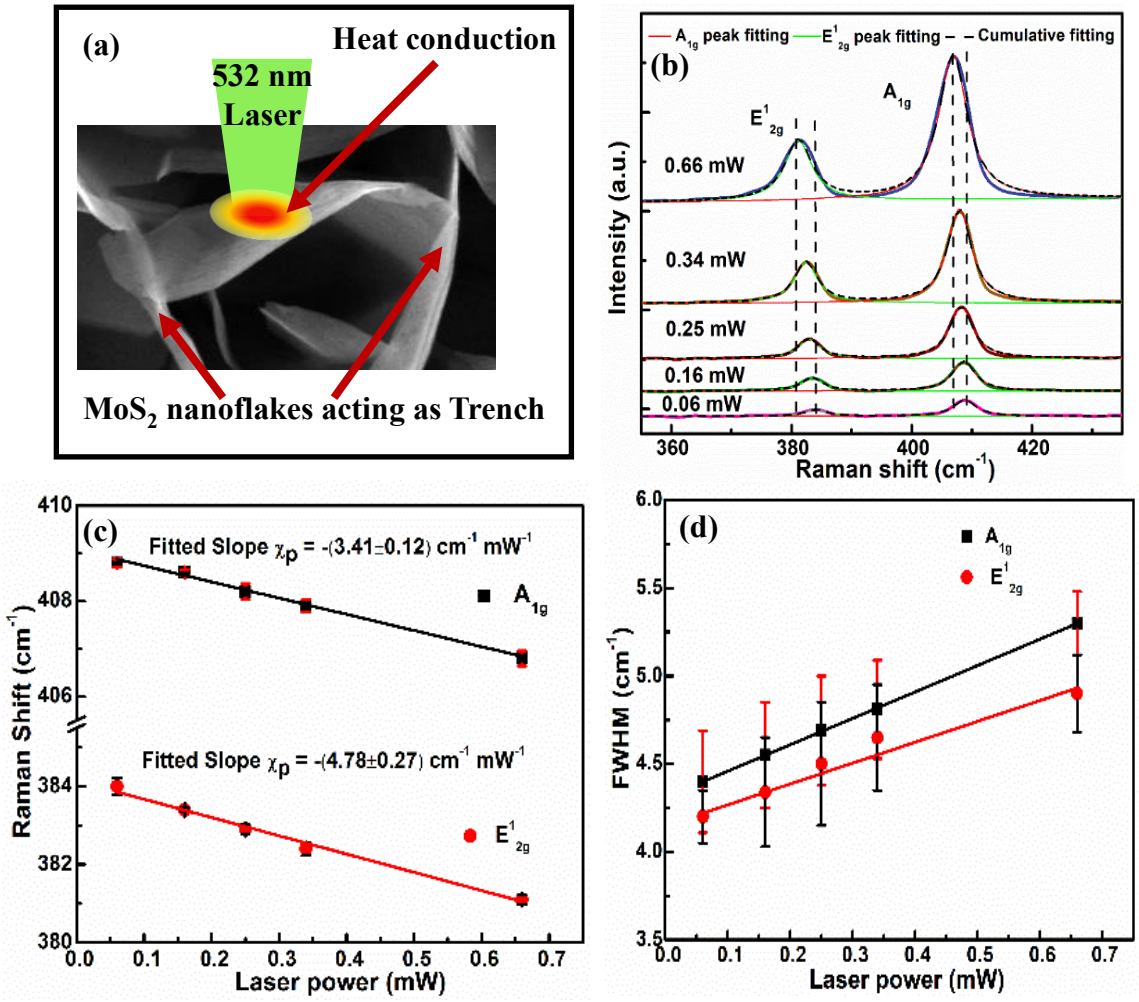

Figure 3.8 *(a) Schematic of heat conduction through VFL-MoS_2 (b) Raman spectra of VFL-MoS_2 at different laser powers (c) Raman shifts and (d) FWHM of E^1_{2g} and A_{1g} modes as a function of laser power.*

Figure 3.8 (b) shows the increase in the intensity of Raman peaks (E^1_{2g} and A_{1g}) with incident laser power and indicates the red shifts in both the Raman modes due to the local temperature rise and hence softening of the bonds [79, 152]. The linear behaviour for the red shifting of both the Raman modes with incident laser power is observed as shown in **Figure 3.8 (c)**. The linear power coefficients χ_P for both modes are calculated from the slopes using **equation 3.10**. In case of VFL-MoS_2, values of χ_P are found to be –3.41±0.12 and –4.78±0.27 cm^{-1} mW^{-1} for A_{1g} and E^1_{2g} modes, respectively. As discussed above, minimal strain effect of substrate in VFL-MoS_2 results in Raman modes sensitivity for laser induced local heating. **Figure 3.8 (d)** shows the variation of FWHM for both the Raman modes indicating that the FWHM increases with incident laser power. The increase of FWHM with respect to laser power occurs because of softening of the bonds and the lattice dilation due to the local heating by laser light [79].

As the strain effect of substrate in VFL-MoS_2 is found minimal, they behave more like suspended nanoflakes. Each of the VFL-MoS_2 nanosheet can be considered as a suspended flake between other two flakes acting as trench for heat sink, as shown schematically in **Figure 3.8 (a)**. The lateral dimension (~ 400 nm) and vertical dimension (~ 500 nm) of our grown VFL-MoS_2 are comparable to the laser Gaussian beam width. Hence, we have calculated the thermal conductivity of the VFL-MoS_2 using the **equation 3.14**. The lateral dimension (2L) of each nanoflake is found around 400 nm (observed in HRSEM image), film thickness (h) about 5 nm (observed in HRTEM image) and width (W) around 500 nm (observed in AFM height profile). Thermal conductivity of VFL-MoS_2 flakes is calculated using χ_T and χ_P values for E^1_{2g} mode. The obtained room temperature in-plane thermal conductivity is found as high as 100 ± 14 W m^{-1} K^{-1}. Thermal conductivities of different MoS_2 nanostructures obtained via OTR study are summarized in **Table-3.1**. The higher thermal conductivity of our VFL-MoS_2 compared

to other MoS_2 nanostructures reported in literature can be attributed to the suspended like behaviour with minimal defects and reduced substrate effect in vertical orientation of MoS_2 [161, 162].

Table 3.1 Thermal Conductivity of MoS_2 Nanostructure with First-Order Temperature Coefficients (χ_T) using OTR Technique.

Nanostructure (Type)	**Mode**	χ_T **($cm^{-1} K^{-1}$)**	**Thermal conductivity ($W m^{-1} K^{-1}$)**	**Reference**
Triangular bi-layer MoS_2 (SiO_2/Si Supported)	A_{1g} E^1_{2g}	−0.011 ± 0.0005 −0.009±0.0003	42.0 ± 8	**Present work**
VFL-MoS_2 (over Si)	E^1_{2g} A_{1g}	−0.012±0.001 −0.011±0.001	100 ± 14	**Present work**
Mono-layer MoS_2 (SiO_2/Si Supported)	A_{1g} E^1_{2g}	−0.012	62.2	ACS. Appl. Mater. Interfaces 2015, **7 (9)**, 5061-5065. [152]
Mono-layer MoS_2 (Au coated SiO_2/Si Supported)	A_{1g} E^1_{2g}	−0.0167 ±0.0007	55 ± 20	ACS Appl. Mater. Interfaces, 2015, **7 (46)**, 25923–25929.[51]
Bi-layer MoS_2 (Au coated SiO_2/Si Supported)	A_{1g} E^1_{2g}	−0.0139 ± 0.0003	35 ± 7	ACS Appl. Mater. Interfaces, 2015, **7 (46)**, 25923–25929.[51]
Few-layer MoS_2 (Suspended)	A_{1g} E^1_{2g}	−0.0123 −0.0132	52	J. Phys. Chem. C, 2013, **117 (17)**,9042–9047.[79]
Mono-layer MoS_2 (Suspended)	A_{1g} E^1_{2g}	−0.013 ± 0.001 −0.011 ± 0.001	34.5 ± 4	ACS Nano, 2014, **8(1)**, 986-993.[78]
Multilayer MoS_2 (Suspended)	A_{1g} E^1_{2g}	−0.0125 −0.0135	43.4 ± 9.1	Nanoscale, 2017, **9 (7)**, 2541–2547.[53]

3.3 Conclusions

In summary, we have successfully grown triangular bi-layer MoS_2 over SiO_2/Si substrate and VFL-MoS_2 over Si substrate via CVD process and examined the phonon confinement effects in prepared MoS_2 films. We have calculated thermal conductivity (k_s) and the interfacial thermal conductance (g) of supported triangular bi-layer MoS_2 by OTR technique and found values of 42 ± 8 W m^{-1} K^{-1} and 1.264 ± 0.128 MW m^{-2} K^{-1} for k_s and g, respectively, suggesting excellent thermal transport properties of prepared bi-layer MoS_2. We report for the first time, thermal conductivity of VFL-MoS_2 using OTR technique and high room temperature in-plane thermal conductivity (~100 ± 14 W m^{-1} K^{-1}) is obtained. The fewer defects and minimal strain in grown VFL-MoS_2 reduce the phonon-defect scattering resulting in high thermal conductivity. This high value of thermal conductivity of prepared MoS_2 films makes it suitable for resolving heating issues like thermal breakdown in electronic and optoelectronic devices.